Renewable Energy, Environment, and Power Quality Journal (REE&PQJ)
ISSN:3020-531X
Volume 24, January 2026

Detecting and Locating Corona Discharges in Low-Pressure Aircraft Environments Using Optical Sensors

P. Bas-Calopa[1], J.-R. Riba[1], and M. Moreno-Eguilaz[2]

[1] Department of Electrical Engineering
Universitat Politècnica de Catalunya
Campus of Terrassa, 08222 Terrassa (Spain)
Phone: +0034 937398365

[2] Department of Electronics Engineering
Universitat Politècnica de Catalunya
Campus of Terrassa, 08222 Terrassa (Spain)
Phone: +0034 937398365

Abstract. Today, there is a clear trend toward electrification of transportation systems, including aircraft. Due to the enormous power requirements, they must operate at high voltages. However, the combined effect of higher voltage levels and low pressure environments is conducive to the occurrence of electrical discharges in electrical systems. Therefore, there is an urgent need to develop cost-effective systems to detect the discharges in the early stages before major failures can occur. This paper compares two optical sensors for early discharge detection in a simulated aircraft environment. The experimental study is performed in a low pressure chamber using a needle plane electrode. The pressure is changed from that corresponding to ground level to that corresponding to flight altitude, i.e., from 100 kPa to 20 kPa. The effect of the supply frequency is also studied, since modern aircraft operate in a wide range of frequencies up to about 800 Hz. Both variables, especially pressure, have shown significant effects on the CIV value. The results have also shown a similar sensitivity of both sensors for all the experimental conditions analysed, allowing a fast and sensitive detection and localization of incipient electrical discharge activity.

Key words. Electrical discharges, corona effect, ultraviolet sensors, electric aircraft, electrical mobility.

1. Introduction

Due to the more efficient use of energy, electric transportation systems are becoming more electrified and are experiencing rapid development. Due to the high power requirements, today's electric vehicles have DC bus voltages of up to 800 V [1]. This is also happening in the aviation industry, which will operate at voltages in excess of such values [2]. This increase in voltage does not come without significant challenges, especially in the harsh environments that characterize aeronautical systems [3]. In particular, the combination of harsh environments and increased voltage levels in more electric aircraft (MEA) and full electric aircraft (FEA) facilitates the occurrence of electrical faults in insulation systems. Electrical systems characteristic of FEA aircraft will operate at high voltages up to 3 kV DC [4], and electrical systems in MEA aircraft today operate in a wide range of frequencies between 300 Hz and 800 Hz [5]. Electrical wiring systems in modern aircraft are complex and compact. In addition, the low-pressure environment in unpressurized areas, rapid changes in altitude and temperature, associated condensation effects, high vibration levels, and exposure to contaminants and UV radiation pose significant challenges to insulation systems. The combination of all these effects favors the occurrence of partial discharge (PD) activity within the insulation of aircraft power wires, leading to insulation degradation and ultimately insulation failure, equipment malfunction and potentially catastrophic failures [6], [7].

The dielectric strength of air is a function of air density and therefore of atmospheric pressure, so the dielectric strength of air decreases with decreasing air density values [8], [9]. In addition, at high altitudes, the reduced air density makes thermal exchange more difficult [10], which poses significant challenges to the behavior of insulation materials and thus favors premature degradation conditions.

For a given voltage level, reduced pressure conditions are known to increase the PD activity, intensity and energy of discharges, thus increasing their potential damage [11]. Thus, insulation systems with no or low PD activity at ground level may fail at flight altitude [12].

Discharge amplitude tends to decrease with pressure, so in low pressure environments, the sensitivity of conventional electromagnetic PD detection methods may not be sufficient [11], so optical detection methods can be of great help because they allow detecting surface PD and corona discharge activity [13], [14]. It is well known that the electrical energy involved in the corona activity is directly related to the intensity of the corona light detected by optoelectronic sensors [15], so that

optoelectronic imaging sensors allow not only the localization of the discharge area, but also the intensity of the discharges.

Solar radiation includes infrared radiation, visible light, ultraviolet (UV) radiation and ionizing radiation of shorter and longer wavelengths, microwaves and radiofrequency, respectively. UV lies in the range of 100–400 nm, being subdivided into UV-A (315–400 nm), UV-B (280–315 nm and UV-C (100–280 nm). Most UV-B and UV-C solar extraterrestrial energy is absorbed by Earth's stratosphere. Solar blind sensors are those that are exclusively sensitive to UV-C wavelengths [16], so they do not generate any signal when exposed to normal sunlight. These sensors can detect the dim UV-C radiation produced by surface and corona discharges, while avoiding sunlight interference [17].

Optical methods, and in particular optoelectronic imaging sensors, are particularly attractive because they allow direct detection and localization of the discharge regions [18], while offering high resolution and sensitivity at a reduced cost and size. They also offer immunity to electromagnetic noise, switching noise, and acoustic noise, so they can be used in transportation systems to detect and locate electrical discharges in their incipient stages, long before irreversible insulation damage occurs.

Optoelectronic imaging sensors, in particular complementary metal-oxide-semiconductor (CMOS) sensors, have undergone extraordinary development with high sensitivity, high resolution and competitive costs. Today, they are widely used in many applications such as digital cameras, camera modules, camera phones, agricultural imaging or medical imaging equipment, among others. Such advances offer promising solutions for corona detection in aeronautical applications.

This study contributes to the field of corona detection for aeronautical applications. Through experiments performed in a low-pressure chamber, the sensitivity of both sensors is compared by determining and comparing the corona inception voltage (CIV) detected by a back-illuminated CMOS and a solar blind UV-C sensor for various atmospheric pressures in the range of 100 to 20 kPa, corresponding to standard atmospheric pressure and the pressure at the flight altitude of commercial aircraft. Experiments are performed using a needle-plane gap in a frequency range from 50 Hz to 800 Hz.

2. Materials

This section describes the materials used in the experimental part.

The corona discharges were generated using a needle-plane geometry. It consists of a stainless steel needle 13 cm long, 1.3 mm in diameter with a hollow tip of 0.03 mm radius and 50° angle placed 20 cm above the ground plane, as shown in Fig. 1.

The experiments were performed with the needle-plane geometry inside a low-pressure chamber. It consists of a cylindrical aluminum tube (250 mm internal diameter, 500 mm height and 6 mm wall thickness) sealed with a methacrylate lid.

The pressure was automatically regulated using a vacuum pump (BA-1, 1/4 HP, 0.085 m^3/min, Bacoeng, Suzhou, China). To regulate the pressure, the pump was connected to an inverter and to a control valve. The pressure level was measured with a digital sensor (PSD-4, -1 bar to 0 bar, ± 0.5%, Wika, Sabadell, Barcelona). The temperature of the inside the chamber was measured with a K-type thermocouple which was connected to a multimeter configured in thermometer mode (Fluke 289 true-RMS multimeter, Fluke, Everett, Washington, WA, USA).

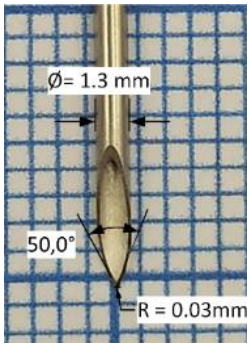

Fig. 1. Needle electrode

The magnitude of the voltage and frequency applied to the needle-plane electrode were controlled by a programmable AC power source (SP300VAC600W, 600 W, 0 - 300 V, ± 0.1 V, 15 - 1000 Hz, APM Technologies, Dongguan, China). The low voltage terminals of a single-phase high voltage transformer (VKPE-36, 600 VA, turns ratio 1:100, maximum voltage 36 kV, Laboratorio Electrotécnico, Cornellà de Llobregat, Spain) were connected to the AC source, while the high voltage terminals were connected to the needle-plane electrode.

The high voltage was measured with a high voltage probe (CT4028, 0 – 39 kV_{peak}, ≤ 3%, 1000:1, DC to 220 MHz, Cal Test Electronics, Yorba Linda, CA, USA) connected to a computer through a data acquisition system (USB-6000 DAQ, 1 kS/s, 12 bits, ≤ ± 26 mV, National Instruments, Austin, TX, USA) as shown in Fig. 2.

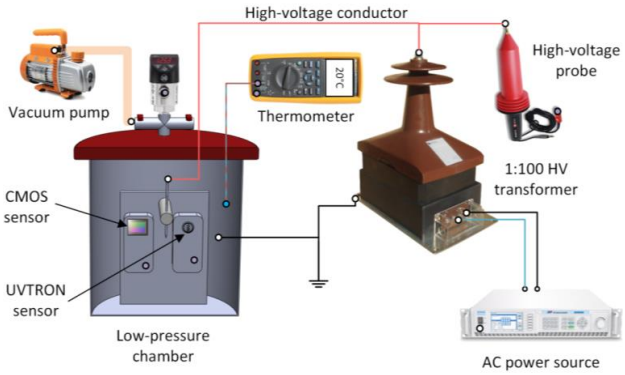

Fig. 2. Sketch of the experimental setup.

Digital images of the corona discharges were acquired using a back-illuminated BI-CMOS imaging sensor (ISOCELL HP2, 1/1.3" sensor size, 0.6 µm cell size, 200 Mpixel resolution, 30 frames/second, manufactured by Samsung, Korea). This BI-CMOS sensor is equipped with a "Tetra²pixel" RGB Bayer Pattern color filter, supports raw format images and is sensitive to both visible and near-UV light.

A head-on solar-blind UV-C sensor (UVtron R9533, Hamamatsu Photonics, Hamamatsu City, Japan) was also used to detect corona UV-C light. The solar-blind sensor

was controlled by an electronic driver (C10807 driver, Hamamatsu Photonics, Hamamatsu City, Japan), which allows the sensor to operate safely while minimizing the probability of false detections. The solar blind sensor is directional, so it was placed inside the low-pressure chamber facing the needle-plane electrode and connected to an external computer via the USB-6000 DAQ device.
The experimental setup was controlled by a Python code written by the authors of this work.
Fig. 3 shows an example of the corona images captured by the BI-CMOS imaging sensor.

Fig. 3. Long-exposure image of a corona discharge on the tip of the needle-plane electrode taken with the BI-CMOS sensor.

3. Method

This section describes the procedure used to experimentally determine the corona inception voltage (CIV) of the needle-plane electrode placed inside the low-pressure chamber.
Fig. 4 describes the flow diagram of the method applied to determine the CIV value.

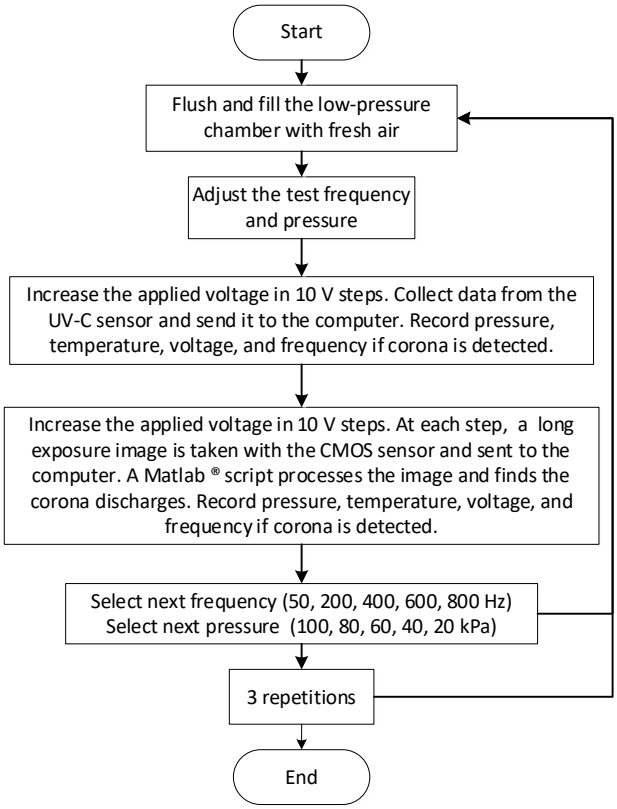

Fig. 4. Process to determine the value of CIV using the three methods of detection.

For a given frequency and pressure, the CIV value resolved by each sensor (solar blind and BI-CMOS sensors) was determined by progressively increasing the high voltage applied to the needle until corona activity was detected by the. Since an iterative procedure was used, a Python code was programmed to control the power source in order to speed up the measurement process. This code automatically sets the frequency of the power supply, adjusts the pressure of the low-pressure chamber to the desired value, increases the voltage, and records the CIV value and other experimental data. Three replicates of each experimental condition were also performed to determine the scatter of the results.

4. Results

Table I summarizes the CIV values obtained by using the solar blind UV-C sensor and the BI-CMOS imaging sensor according to the experimental setup shown in Fig. 2 when analysing different frequencies (50 Hz, 200 Hz, 400 Hz, 600 Hz, 800 Hz and 1000 Hz) and different pressures (100 kPa, 80 kPa, 60 kPa, 40 kPa and 20 kPa).

Table I. Experimental CIV values for the needle- plane electrode geometry versus pressure and supply frequency

		UV sensor			BI-CMOS sensor		
Press.	Freq.	Mean value	Min	Max	Mean value	Min	Max
100 kPa	50 Hz	2.934	2.872	2.967	2.889	2.818	2.934
	200 Hz	2.799	2.749	2.844	2.719	2.655	2.816
	400 Hz	2.741	2.712	2.773	2.737	2.641	2.786
	600 Hz	2.703	2.671	2.767	2.781	2.751	2.834
	800 Hz	2.672	2.619	2.777	2.759	2.715	2.846
80 kPa	50 Hz	2.512	2.397	2.579	2.562	2.452	2.628
	200 Hz	2.425	2.383	2.493	2.485	2.441	2.555
	400 Hz	2.397	2.372	2.447	2.387	2.355	2.433
	600 Hz	2.355	2.305	2.446	2.434	2.392	2.518
	800 Hz	2.363	2.325	2.436	2.379	2.361	2.413
60 kPa	50 Hz	2.112	2.041	2.164	2.091	1.998	2.182
	200 Hz	2.065	2.045	2.103	2.061	1.993	2.161
	400 Hz	2.020	1.968	2.084	2.072	2.028	2.124
	600 Hz	2.027	1.987	2.086	2.086	2.064	2.129
	800 Hz	2.022	1.984	2.096	2.056	2.031	2.069
40 kPa	50 Hz	1.673	1.666	1.685	1.672	1.632	1.716
	200 Hz	1.626	1.602	1.657	1.683	1.658	1.715
	400 Hz	1.627	1.599	1.682	1.657	1.640	1.672
	600 Hz	1.629	1.588	1.691	1.664	1.657	1.676
	800 Hz	1.631	1.581	1.688	1.669	1.651	1.701
20 kPa	50 Hz	1.169	1.152	1.188	1.186	1.118	1.231
	200 Hz	1.140	1.121	1.158	1.185	1.155	1.227
	400 Hz	1.156	1.144	1.179	1.197	1.177	1.217
	600 Hz	1.143	1.127	1.170	1.189	1.185	1.191
	800 Hz	1.150	1.134	1.180	1.209	1.186	1.236

For a better visualization of the data, the results presented in Table I have been plotted in Fig. 5.

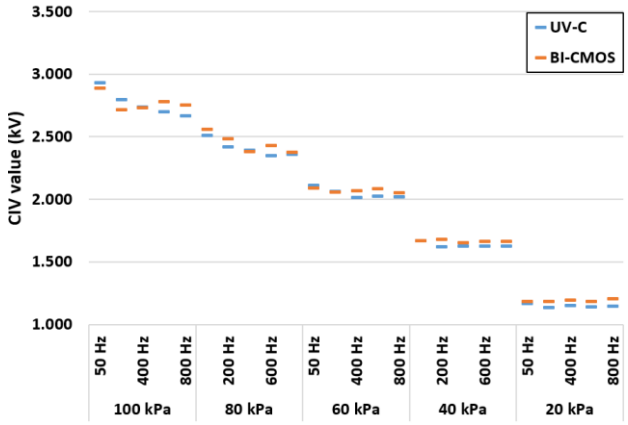

Fig. 5. CIV values performed for the needle-plane electrode geometry detected by the UV-C and the BI-CMOS sensor for various atmospheric pressures and supply frequencies.

The results presented in Fig. 5 clearly show that as predicted by Peek [19] and Paschen's laws, the CIV values obviously decrease with decreasing values of atmospheric pressure. They also show that the CIV value tends to decrease with increasing power frequency, although this dependence is less pronounced and in some cases within the experimental inaccuracies and variability inherent in the complex corona behaviour. Other previous work has also reported this trend [20]. The results presented in Fig. 5 also show that the effect of frequency decreases as the atmospheric pressure reduces.

Finally, Table II illustrates the difference in CIV values as measured by the UV sensor versus the BI-CMOS sensor. Note that positive values in Table II indicate that the UV-C sensor requires a higher voltage than the BI-CMOS to detect the CIV, in this case indicating a smaller sensitivity, while negative values indicate a higher sensitivity of the UV-C sensor.

Table II. Percentage difference in the CIV values measured by both sensors for each frequency-pressure level using the needle-plane geometry.

	Air pressure					
	100 kPa	**80 kPa**	**60 kPa**	**40 kPa**	**20 kPa**	
50 Hz	1.53%	-1.95%	1.02%	0.02%	-1.49%	**-0.17%**
200 Hz	2.95%	-2.44%	0.18%	-3.37%	-3.83%	**-1.30%**
400 Hz	0.15%	0.45%	-2.54%	-1.79%	-3.43%	**-1.43%**
600 Hz	-2.82%	-3.27%	-2.84%	-2.10%	-3.9%	**-2.99%**
800 Hz	-3.15%	-0.67%	-1.65%	-2.30%	-4.88%	**-2.53%**
	-0.27%	**-1.58%**	**-1.17%**	**-1.91%**	**-3.51%**	
	Column average					

Row average

The data summarized in Table II indicate subtle differences in sensor sensitivity, with the UV-C sensor exhibiting slightly higher sensitivity compared to the BI-CMOS sensor, especially at low pressure and higher frequency operation.

It should be noted that the UV-C sensor provides a frequency signal proportional to the intensity of the detected UV-C light, but it is not an imaging sensor. This means that this sensor is able to detect the corona activity and the approximate direction of the UV-C light, but does not allow the exact location of the corona source. In contrast, the BI-CMOS imaging sensor can do both, determining the intensity of the corona activity and the exact localization of the corona source.

4. Conclusion

This experimental study investigated the influence of pressure and frequency on visual corona detection using a solar blind UV-C sensor and a BI-CMOS imaging sensor. A needle-plane electrode geometry was analysed that was placed in a low-pressure chamber to reproduce the low-pressure environment characteristic of aircraft flight altitudes. In addition to the pressure, which was studied in the range of 20 - 100 kPa, the frequency of the power supply was varied from 50 Hz to 800 Hz. Both variables, especially the pressure, have shown important effects on the CIV value. The results show a significant decrease in CIV with decreasing air pressure, such that in the 100-20 kPa range, the CIV decreases by approximately a factor of 2.5:1. Frequency also has an effect on the CIV, but it is much smaller, so that the CIV tends to decrease with increasing frequency. The effect of frequency also decreases with atmospheric pressure.

Both sensors showed a very similar sensitivity, i.e. they provided very similar CIV values for all analysed experimental conditions. The solar blind UV-C sensor performed slightly better than the BI-CMOS sensor at higher frequencies and lower pressures.

Finally, it should be noted that the UV-C sensor provides a frequency signal proportional to the intensity of the detected UV-C light, but does not allow direct localization of the corona source. In contrast, the BI-CMOS imaging sensor provides a direct and accurate localization of the corona source.

Acknowledgement

This research was partially funded by Ministerio de Ciencia e Innovación de España, grant number PID2020-114240RB-I00 and by the Generalitat de Catalunya, grant number 2021 SGR 00392.

References

[1] A. Allca-Pekarovic, P. J. J. Kollmeyer, P. Mahvelatishamsabadi, T. Mirfakhrai, P. Naghshtabrizi, and A. Emadi, "Comparison of IGBT and SiC Inverter Loss for 400V and 800V DC Bus Electric Vehicle Drivetrains," in *ECCE 2020 - IEEE Energy Conversion Congress and Exposition*, 2020, pp. 6338–6344.

[2] J.-R. Riba, M. Moreno-Eguilaz, T. Ibrayemov, and M. Boizieau, "Surface Discharges Performance of ETFE- and PTFE-Insulated Wires for Aircraft Applications," *Mater. 2022, Vol. 15, Page 1677*, vol. 15, no. 5, p. 1677, Feb. 2022.

[3] B. Sarlioglu and C. T. Morris, "More Electric Aircraft: Review, Challenges, and Opportunities for Commercial Transport Aircraft," *IEEE Trans. Transp. Electrif.*, vol. 1, no. 1, pp. 54–64, 2015.

[4] H. El Bayda *et al.*, "Energy losses from an arc tracking in

aeronautic cables in DC circuits," *IEEE Trans. Dielectr. Electr. Insul.*, vol. 20, no. 1, pp. 19–27, Feb. 2013.
[5] "ISO 1540:2006 Aerospace — Characteristics of aircraft electrical systems." p. 56, 2006.
[6] "What Are the Disadvantages of Kapton Insulated Wire? - InterConnect Wiring." .
[7] J.-R. Riba, M. Moreno-Eguilaz, and J. A. Ortega, "Arc Fault Protections for Aeronautic Applications: A Review Identifying the Effects, Detection Methods, Current Progress, Limitations, Future Challenges, and Research Needs," *IEEE Trans. Instrum. Meas.*, p. 1, 2022.
[8] L. Lusuardi, A. Rumi, A. Cavallini, D. Barater, and S. Nuzzo, "Partial Discharge Phenomena in Electrical Machines for the More Electrical Aircraft. Part II: Impact of Reduced Pressures and Wide Bandgap Devices," *IEEE Access*, vol. 9, pp. 27485–27495, 2021.
[9] J.-R. Riba, Á. Gómez-Pau, and M. Moreno-Eguilaz, "Experimental Study of Visual Corona under Aeronautic Pressure Conditions Using Low-Cost Imaging Sensors," *Sensors*, vol. 20, no. 2, p. 411, Jan. 2020.
[10] R. Hosseini and H. Taherian, "Natural convection heat transfer from a vertical plate to air at very low pressure," *Trans. Can. Soc. Mech. Eng.*, vol. 28, no. 2 B, pp. 309–319, 2004.
[11] L. Lusuardi, A. Rumi, G. Neretti, P. Seri, and A. Cavallini, "Assessing the severity of partial discharges in aerospace applications," in *Annual Report - Conference on Electrical Insulation and Dielectric Phenomena, CEIDP*, 2019, pp. 267–270.
[12] A. Rumi, J. G. G. Marinelli, D. Barater, A. Cavallini, and P. Seri, "The Challenges of Reliable Dielectrics in Modern Aerospace Applications: The Hazard of Corona Resistant Materials," *IEEE Trans. Transp. Electrif.*, vol. 8, no. 4, pp. 4646–4653, Dec. 2022.
[13] D. Ma, L. Jin, J. He, and K. Gao, "Classification of partial discharge severities of ceramic insulators based on texture analysis of UV pulses," *High Volt.*, vol. 6, no. 6, pp. 986–996, Dec. 2021.
[14] P. Bas-Calopa, J. R. Riba, and M. Moreno-Eguilaz, "Corona Discharge Characteristics under Variable Frequency and Pressure Environments," *Sensors 2021, Vol. 21, Page 6676*, vol. 21, no. 19, p. 6676, Oct. 2021.
[15] J.-R. Riba, Á. Gómez-Pau, and M. Moreno-Eguilaz, "Insulation Failure Quantification Based on the Energy of Digital Images Using Low-Cost Imaging Sensors," *Sensors*, vol. 20, no. 24, 2020.
[16] P. Schreiber, T. Dang, T. Pickenpaugh, G. A. Smith, P. Gehred, and C. W. Litton, "Solar-blind UV region and UV detector development objectives," in *Optoelectronics '99 - Integrated Optoelectronic Devices*, 1999, vol. 3629, pp. 230–248.
[17] J.-R. Riba, M. Moreno-Eguilaz, M. Boizieau, and T. Ibrayemov, "Performance Evaluation of Solar-Blind Gas-Filled Sensors to Detect Electrical Discharges for Low-Pressure Aircraft Applications," *Sensors 2022, Vol. 22, Page 492*, vol. 22, no. 2, p. 492, Jan. 2022.
[18] Z. Guo, Q. Ye, F. Li, and Y. Wang, "Study on corona discharge spatial structure and stages division based on visible digital image colorimetry information," *IEEE Trans. Dielectr. Electr. Insul.*, vol. 26, no. 5, pp. 1448–1455, Oct. 2019.
[19] F. W. Peek, "The law of corona and the dielectric strength of air," *Proc. Am. Inst. Electr. Eng.*, vol. 30, no. 7, pp. 1485–1561, 1911.
[20] W. Linder and H. Steele, "Estimating voltage breakdown performance of high-altitude antennas," in *WESCON/59 Conference Record*, 1959, vol. 3, pp. 9–16.